ARTICLE IN PRESS

Nature Communications

https://doi.org/10.1038/s41467-026-71748-7

Article in Press

A plant-receptor-inspired cuprous complex for wearable trace-level ethylene gas sensing

Received: 25 July 2025

Accepted: 25 March 2026

Cite this article as: Xu, L., Zhang, B., Tang, B. *et al.* A plant-receptor-inspired cuprous complex for wearable trace-level ethylene gas sensing. *Nat Commun* (2026). https://doi.org/10.1038/s41467-026-71748-7

Lulu Xu 露露, Bohai Zhang 渤海, Bin Tang 唐, Han Xu 徐涵, Hao Zhang 浩, Zhiqi Zhao 志奇, Yijun Liu 刘奕君, Xingyu Chen 星宇, Lanlan Li 李, Jiandong Hu 胡建, Zhen Zhou 周震 & Junfeng Wu 吴俊

We are providing an unedited version of this manuscript to give early access to its findings. Before final publication, the manuscript will undergo further editing. Please note there may be errors present which affect the content, and all legal disclaimers apply.

If this paper is publishing under a Transparent Peer Review model then Peer Review reports will publish with the final article.

ARTICLE IN PRESS

© The Author(s) 2026. **Open Access** This article is licensed under a Creative Commons Attribution-NonCommercial-NoDerivatives 4.0 International License, which permits any non-commercial use, sharing, distribution and reproduction in any medium or format, as long as you give appropriate credit to the original author(s) and the source, provide a link to the Creative Commons licence, and indicate if you modified the licensed material. You do not have permission under this licence to share adapted material derived from this article or parts of it. The images or other third party material in this article are included in the article's Creative Commons licence, unless indicated otherwise in a credit line to the material. If material is not included in the article's Creative Commons licence and your intended use is not permitted by statutory regulation or exceeds the permitted use, you will need to obtain permission directly from the copyright holder. To view a copy of this licence, visit http://creativecommons.org/licenses/by-nc-nd/4.0/.

A Plant-receptor-inspired Cuprous Complex for Wearable Trace-level Ethylene Gas Sensing

Lulu Xu (许露露)[1,†], Bohai Zhang (张渤海)[2,3,†], Bin Tang (唐宾)[3,4], Han Xu (徐涵)[2], Hao Zhang (张浩)[1], Zhiqi Zhao (赵志奇)[1], Yijun Liu (刘奕君)[1], Xingyu Chen (陈星宇)[1], Lanlan Li (李兰兰)[1], Jiandong Hu (胡建东)[1,*], Zhen Zhou (周震)[4,*], Junfeng Wu (吴俊锋)[1,*]

[1] Henan International Joint Laboratory of Laser Technology in Agriculture Sciences, College of Mechanical & Electrical Engineering, Henan Agricultural University, Zhengzhou, Henan, P. R. China.

[2] Flavors and Fragrance Engineering & Technology Research Center of Henan Province, College of Tobacco Science, Henan Agricultural University, Zhengzhou, Henan, P. R. China.

[3] Key Laboratory of Advanced Energy Materials Chemistry (Ministry of Education), Nankai University, Tianjin, P. R. China.

[4] Interdisciplinary Research Center for Sustainable Energy Science and Engineering, School of Chemical Engineering, Zhengzhou University, Zhengzhou, Henan, P. R. China.

[†] These authors contributed equally: Lulu Xu, Bohai Zhang

[*] Corresponding author email: Jiandong Hu, jdhu@henau.edu.cn; Zhen Zhou, zhouzhen@nankai.edu.cn; Junfeng Wu, jfwu@henau.edu.cn

Abstract

Ethylene (C_2H_4) functions both as a key phytohormone regulating plant growth and development and as an essential feedstock in organic chemical synthesis. Reliable detection of C_2H_4 is critical for monitoring emissions during crop cultivation and ensuring safety in industrial transportation. However, most existing C_2H_4 sensors rely on noble-metal catalysts and/or high-operating temperature, which significantly constrain their practical applications. Moreover, achieving high specificity in C_2H_4 recognition remains a major challenge. Inspired by the signal transduction mechanism of plant C_2H_4 receptor, this study propose a biomimetic sensing strategy based on a facilely synthesized cuprous-cystine complex (Cu_2Cyt), which features a sulfur-bridged Cu^+ coordination center that mimics the biological binding site for C_2H_4 recognition. The noble-metal-free wearable sensor was fabricated by depositing a Cu_2Cyt/MXene composite onto a flexible interdigital electrode, enabling room-temperature detection of C_2H_4 emitted from fruits or leaked from transport pipelines of chemical industries. It exhibits a detection range (0.05-5 ppm), an ultra-low detection limit of 1.07 ppb, fast response/recovery (51/92 s), high sensitivity of 3.64%·ppm^{-1} in trace concentration range of 0-0.5 ppm, and good reversibility and reproducibility. Overall, this work offers a bioinspired design strategy for low-cost, high-performance, noble-metal-free, and wearable sensors, capable of trace-level C_2H_4 monitoring.

Keywords: Trace-level ethylene sensing; Biomimetic wearable sensors; Room-temperature detection; Noble-metal-free composite; MXene

Introduction

Ethylene (C_2H_4) plays a dual role as both a pivotal plant hormone regulating growth and development, and as one of the most widely produced industrial chemicals, primarily used in the manufacture of plastics and polymers[1,2]. In the agricultural field, understanding C_2H_4 dynamics is essential for optimizing harvest timing, improving storage conditions, and enabling early detection of spoilage or stress-induced responses. Meanwhile, in industrial settings, unintended C_2H_4 leakage from transportation pipeline not only leads to resource loss but also poses safety risks[3]. Therefore, the development of a highly sensitive and selective C_2H_4 detection system holds significant value for postharvest quality control, plant physiological research, and safety management in chemical industries.

Traditional C_2H_4 detection technologies, such as gas chromatography (GC)[4], fluorescence spectroscopy[5], and photoacoustic spectroscopy[6], offer high analytical precision. However, their reliance on bulky instrumentation, labor-intensive sample preparation, and stringent operational conditions greatly limits their feasibility for real-time and in-situ applications[7,8]. To overcome these limitations, various sensor-based approaches have been developed, including metal oxide semiconductor[9], electrochemical[10], and quartz crystal microbalance sensors[11]. While each exhibits specific advantages, most conventional C_2H_4 sensors suffer from inherent drawbacks such as mechanical rigidity, high operating temperature, and limited long-term durability. These characteristics hinder their integration into wearable platforms required for low-cost distributed deployment in smart agriculture and industrial pipeline monitoring[12].

Chemiresistive sensors detect target gases by monitoring changes in the electrical resistance of sensing materials in response to varying gas concentrations[13,14]. Owing to their simple architecture, fast response, ease of miniaturization, and low manufacturing cost, these sensors have gained widespread use, especially in wearable and portable gas-sensing devices[15,16]. A wide array of sensing materials has been employed in chemiresistive platforms, including carbon-based nanomaterials (such as carbon nanotubes and graphene), conductive polymers (such as polyaniline and polypyrrole), and emerging two-dimensional materials such as MoS_2 and MXenes[17,18]. Although the general sensing mechanisms are well understood, the specific pathways through which environmental factors (such as humidity and oxygen) interfere with sensor performance remain unclear. Moreover, high-cost noble metal catalysts (such as Pd, Pt, Ru) are commonly incorporated to enhance response and sensitivity via the Wacker-type oxidation mechanism[19-21]. Some low-cost catalysts, including catalytic overlayer (such as Cr_2O_3)[22] and metal-organic complexes[23] have also been explored to enhance surface oxidation and facilitate charge transfer upon C_2H_4 adsorption. Nevertheless, these catalytic systems involved oxidation mechanism often suffer from poor selectivity, particularly for reducing gases, thereby restricting their applicability in complex environments.

Recent studies have demonstrated the unique specificity and affinity of copper(I) compounds (such as Cu_2O and Cu^+-based metal-organic frameworks) toward C_2H_4, primarily due to the stable π-complexation between Cu^+ and the C=C double bond in C_2H_4[24-26]. These findings position Cu^+ as a highly effective active center for selective C_2H_4 detection. This chemical specificity finds a remarkable parallels in plant biology, where C_2H_4 receptor proteins localized on the endoplasmic reticulum serve as evolutionarily optimized modules for C_2H_4 recognition[27,28]. The primary recognition center is widely considered to be disulfide-linked homodimers coordinated with chelating Cu^+ cofactors. Such biological precision in trace C_2H_4 recognition offers compelling biomimetic inspiration for the development of Cu^+-mediated wearable sensing technologies. In fact, a coordination compound structurally analogous to the biological recognition center has been chemically synthesized using L-Cysteine thiol and $CuCl_2$ in defined stoichiometric ratios[29,30]. Leveraging this concept, bioinspired functional interfaces that mimic natural receptor structures represent a promising strategy for developing high-selectivity C_2H_4 sensors.

In this work, we present a biomimetic strategy for selective C_2H_4 recognition, inspired by plant receptor. As illustrated in Fig. 1, a Cu^+ coordination complex (cuprous cystine, Cu_2Cyt) with a peony-like morphology (Fig. 1a) was rationally designed to mimic the Cu^+-coordinated active center of plant C_2H_4 receptors (Fig. 1b). To construct the sensing platform, MXene, a p-type two-dimensional semiconductor material, was employed as a conductive substrate to form a heterojunction with Cu_2Cyt. Upon C_2H_4 binding, the formation of a $Cu_2Cyt(C_2H_4)$ complex induces electron transfer (ET) from the complex to MXene substrate, in which this process reduces the hole carrier density within MXene, resulting in a measurable increase in its electrical resistance. Such biomimetic recognition mechanism enables a concentration-dependent resistance response at room temperature, without the use of noble-metal catalysts. The sensing composite was integrated onto a flexible interdigital electrode (IDE) and systematically evaluated in performance. Furthermore, the sensing mechanism was elucidated through a combination of spectral analyses, theoretical calculations, and a response model that integrates Langmuir gas adsorption theory with semiconductor principles. Overall, this work demonstrates the successful translation of biological recognition principles into material design, offering a pathway for the development of low-cost, room-temperature, and wearable C_2H_4 sensors.

Results

The morphology and structure of sensing materials have an important effect on the performance of sensors. Scanning electron microscopy (SEM) revealed that the as-synthesized Cu_2Cyt exhibits a peony flower-like architecture composed of micrometer-sized clusters (Fig. 2a, b). These clusters are assembled from nanoscale petal-like sheets containing carbon (C), nitrogen (N), copper (Cu), oxygen (O), and sulfur (S) elements (Fig. 2c). Nanosheets significantly increase the surface-to-volume ratio, while the open, petal-shaped configuration enhances the accessibility of target C_2H_4 molecules. To facilitate ET upon C_2H_4 binding, Cu_2Cyt was composited with a small amount of two-dimensional MXene possessing a wrinkled morphology (Fig. S1). The resulting Cu_2Cyt/MXene composite retains the characteristic flower-like morphology of Cu_2Cyt (Fig. 2d), with MXene distributed around the Cu_2Cyt clusters, as highlighted by the white-dotted region. The hierarchical structure is well-preserved (Fig. 2e), ensuring effective gas diffusion and adsorption. Elemental mapping of Ti (from MXene) further confirms the surface location of Cu_2Cyt clusters atop the MXene background (Fig. 2f).

Low-magnification SEM images of the Cu_2Cyt/MXene composites reveal the arrangement of multiple microflowers (Fig. S2a–b), indicating good structural uniformity on a larger scale. A side-view SEM image of an individual microflower is also provided to elucidate its internal composition and architecture (Fig. 2g). The structure forms a well-connected three-dimensional network composed of branched and sheet-like units with open channels, without noticeable aggregation or densely packed regions (Fig. 2h). Elemental mapping of a cross-sectional region further shows the presence of Ti within the interior of the microflowers (Fig. 2i), confirming that MXene, as a conductive component, is interwoven with Cu_2Cyt nanosheets throughout the structure. This hierarchical porous architecture and cross-distributed composition create efficient pathways for gas diffusion and electron transport, thereby exposing more active sites and enhancing the sensing response.

High-magnification SEM images reveal neat petal edges with individual sheet thicknesses of *ca.* 50-100 nm (Fig. 2j). The smooth overlapping nanosheets form a porous network with nanoscale inter-sheet gaps, enabling gas molecules to access both external and internal surfaces. The N_2 adsorption–desorption isotherms (Fig. S3) show that Cu_2Cyt and Cu_2Cyt/MXene composites possess BET surface area of 7.07 and 11.55 $m^2 \cdot g^{-1}$ respectively. The slight increase confirms that a small amount of MXene effectively enhances the accessible surface area without disrupting the structural integrity. Notably, the characteristic of Cu_2Cyt nanosheets accords with the requirement for the assumptions of Langmuir gas adsorption model, *i.e.*, a uniform planar surface with no intermolecular interactions, dynamic equilibrium governed by partial pressure and surface coverage[31,32].

High-resolution transmission electron microscope (HR-TEM) was employed to investigate the crystalline features of the petal-like Cu_2Cyt structures. As shown in Fig. 2k, faint lattice fringes were observed, with interplanar spacings of 0.231, 0.282, 0.289 nm, indicating the presence of partially ordered domains within the otherwise amorphous or low-crystalline matrix. To further elucidate the crystal structure, X-ray diffraction (XRD) patterns were recorded for commercial L-Cysteine, the synthesized Cu_2Cyt, and Cu_2Cyt/MXene composite (Fig. 2l). The diffraction pattern of L-Cysteine matches well with the reference standard card (PDF #32-1636), confirming its phase purity. In contrast, Cu_2Cyt exhibits a distinct set of diffraction peaks that differ from L-Cysteine but partially align with those of L-Cystine — the oxidized disulfide dimer of L-Cysteine — corresponding to the (100), (0018), (112) and (201) crystal planes of L-Cystine (PDF #37-1802). This suggests that Cu_2Cyt adopts a structural motif analogous to L-Cystine, likely retaining the disulfide bond (S–S) as a bridging ligand in the Cu^+ coordination environment. Moreover, the characteristic peaks of Cu_2Cyt remain visible in the Cu_2Cyt/MXene composite, with increased intensity (Fig. S4), indicating that the incorporation of a small amount of MXene enhances the crystallinity of Cu_2Cyt and endows interaction between them. This also supports the conclusion that Cu_2Cyt is distributed on the surface of MXene, in agreement with the SEM and elemental mapping results discussed earlier.

The Cu_2Cyt complex was synthesized via the reaction between L-Cysteine and $CuCl_2$ under alkaline conditions, as detailed in Methods section. In this system, NaOH promotes the deprotonation of the thiol group (–SH) in L-Cysteine, generating a thiolate anion ($–S^–$) with enhanced nucleophilicity for Cu^{2+}

coordination. Due to the oxidizing nature of Cu^{2+}, the $–S^−$ simultaneously acts as a reducing agent, converting Cu^{2+} to Cu^+ while being oxidized to form a S–S. The overall reaction is shown in Fig. 3a: $2C_3H_7NO_2S + 4OH^- + 2Cu^{2+} \rightarrow Cu_2C_6H_{10}N_2O_4S_2\downarrow + 4H_2O$. The standard Gibbs free energy of this reaction was calculated to be -22.92 eV at B3LYP/def2-TZVP level of theory with Grimme's D3 dispersion correction and Becke-Johnson damping, using Gaussian 16 program[33], suggesting the process is thermodynamically favorable. The optimized structure of Cu_2Cyt reveals that one Cu^+ is coordinated to the carbonyl oxygens of the two carboxyl groups (–C=O), as well as to the nitrogen atom of the amino group ($–NH_2$) and the sulfur atom of the cystine-derived disulfide bridge. The second Cu^+ ion coordinates with the carbonyl oxygen of a single C=O and the amino nitrogen, forming a stable chelate structure resembling the C_2H_4-binding domain of plant C_2H_4 receptor.

To experimentally validate the formation mechanism of Cu_2Cyt, molecular spectroscopy techniques were employed to analyze the relevant reactants and products. Raman spectra reveal the disappearance of the characteristic –SH stretching peak of L-Cysteine, accompanied by the appearance of a signal assigned to the S–S bond in Cu_2Cyt (Fig. 3b). This confirms that L-Cysteine undergoes oxidative dimerization via S–S linkage, forming a cystine-like molecular structure. Fourier transform infrared (FTIR) spectroscopy was further conducted to probe vibrational changes associated with functional group conversion and coordination interactions (Fig. S5). In the FTIR spectrum of L-Cysteine, bands at ~1540 cm^{-1} and ~1585/1395 cm^{-1} correspond to the bending vibration of $–NH_3^+$ and the asymmetric/symmetric stretching of $–COO^−$, respectively[34], reflecting its internal protonation of molecules. In commercial L-Cystine sample, there are similar bands at ~1621.9 cm^{-1} (symmetry bending vibration of $–NH_3^+$) and ~1581.1/1406.7 cm^{-1} (the asymmetric/symmetric stretching of $–COO^−$) due to internal protonation of molecules, as shown in Fig. 3c. Nevertheless, the spectrum of the prepared Cu_2Cyt shows the disappearance of the $–NH_3^+$ bending band and the emergence of a signal assigned to $–NH_2$ bending at 1619.7 cm^{-1}, indicating that the ammonium group is deprotonated under alkaline conditions during complexation.

Notably, the majority of peaks of the prepared Cu_2Cyt are consistent with those of L-Cystine sample, while several different points exist due to Cu coordination. Because transition metal atoms are relatively heavy, the related vibrations should be in the low-frequency region[35], as shown in the enlarged area of Fig. 3c. Compared with L-Cystine, three peaks for Cu_2Cyt newly emerge at 518.4, 502.5, and 489.9 cm^{-1}, which are attributed to Cu–O, Cu–N, Cu–S coordination vibrations[36,37], respectively, suggesting the formation of Cu-ligand bonds. In addition, the bending vibration of $–COO^-$ in Cu_2Cyt exhibits a redshift compared with that of L-Cystine, indicating that it is the heavier Cu(I) coordination in Cu_2Cyt while it is the lighter $–NH_3^+$ coordination in L-Cystine. Furthermore, the redshift observed in the $–COO^-$ bending vibration of Cu_2Cyt, compared with that in L-Cystine, signifies the difference in cation coordination: the heavier Cu(I) coordinates in Cu_2Cyt, whereas the lighter $–NH_3^+$ is involved in L-Cystine. These spectral features are consistent with the coordination structure predicted by DFT calculations, further corroborating the proposed binding mode of Cu^+ with the $–COO^-$, $–NH_2$, and –S–S– in the Cu_2Cyt complex.

X-ray photoelectron spectroscopy (XPS) was employed to investigate the elemental composition and chemical state of Cu_2Cyt and Cu_2Cyt/MXene composite. The survey spectrum of Cu_2Cyt confirms the presence of C, N, O, S, and Cu elements, while an additional Ti signal is observed in the Cu_2Cyt/MXene sample, originating from the MXene component. This is consistent with the elemental distribution observed in SEM-EDS mapping (Fig. S6). The high-resolution Cu *2p* spectrum (Fig. 3d) displays two distinct peaks at 931.4 eV and 951.4 eV, corresponding to Cu $2p_{3/2}$ and Cu $2p_{1/2}$, respectively. The absence of satellite peaks between them suggests that the copper species predominantly exist in the +1 or 0 oxidation states—Cu(I) or Cu(0) — rather than Cu(II). Electron paramagnetic resonance (EPR) measurements were further conducted to support this conclusion (Fig. S7). As expected, no signal corresponding to paramagnetic Cu(II), which has an [Ar]$3d^9$ electron configuration, is observed within the magnetic field range of 3000–3500 G[38]. In contrast, Cu(I) possesses a diamagnetic [Ar]$3d^{10}$ configuration, and therefore its absence in the EPR spectrum is consistent with its electronic structure. Given the negligible binding energy difference (approximately 0.1 eV) between Cu(I) and Cu(0)[39], it is difficult to unambiguously distinguish them by XPS alone. However, no characteristic metallic red color associated with Cu(0) was observed during synthesis. Instead, the as-prepared Cu_2Cyt appeared as a milky yellow suspension, yielding a white precipitate after washing and centrifugation (inset of Fig. 3d). These visual observations, in agreement with prior reports[30], support the assignment of Cu(I) as the dominant oxidation state in the metal complex.

The high-resolution S *2p* spectrum of Cu_2Cyt (Fig. 3e) shows two peaks at 163.4 eV and 164.5 eV, attributable to S $2p_{3/2}$ and S $2p_{1/2}$ of the S–S bond[40], consistent with Raman results confirming oxidative dimerization of thiols. After mixing with MXene, the high-resolution C *1s* spectrum of Cu_2Cyt (Fig. 3f) shows no significant shift in the binding energies of the C=O, C–O, C–N/C–S (Fig. S8), indicating that the chemical environment of Cu_2Cyt remains unchanged. This suggests that the interaction between Cu_2Cyt and MXene is primarily physical rather than covalent. To determine the semiconducting nature of MXene, Mott-Schottky analysis was performed (Fig. S9), which can reveal the relationship between the space charge layer capacitance and the applied potential (E)[41]. The resulting plot exhibits a negative slope (Fig. S10), confirming the p-type semiconductor behavior of MXene, which is crucial for facilitating hole modulation upon ET from the Cu_2Cyt sensing layer.

The adsorption of C_2H_4 onto Cu_2Cyt is a key factor influencing the selectivity of Cu(I)-based sensing systems. As the Cu_2Cyt molecule contains two Cu^+ centers capable of π-complexation with C_2H_4, the Gibbs free energy changes (ΔG_{ads}) for the adsorption of one and two C_2H_4 molecules were calculated to be -1.07 eV and -1.51 eV, respectively (Fig. 4a), indicating that dual-site adsorption is thermodynamically more favorable. In this process, the electron-rich C=C double bond of C_2H_4 interacts with the electron-deficient Cu^+ centers, forming a π-complex through coordination. These results provide theoretical support for the high affinity of Cu_2Cyt toward C_2H_4, confirming its potential as an effective sensing material. Detailed computational methods are provided in Section S2 of Supplementary Information. This specific binding mode mimics the C_2H_4 recognition mechanism found in plant receptor, wherein cysteine residues coordinate to chelated Cu^+ ions to enable selective and sensitive detection.

Fig. 4b presents the charge redistribution behavior among MXene, Cu_2Cyt, and C_2H_4 after C_2H_4 adsorption. A decrease in charge density is observed around 15 Å, corresponding to the spatial position of the C_2H_4 molecule, indicating electron donation from the C=C π-system to the Cu_2Cyt complex. Concurrently, an increase in charge density in charge density near 14 Å, aligned with the Cu^+ site, confirms that these electrons are partially accepted by the Cu^+ center. Additionally, an increase in charge density is observed at approximately 8 Å, corresponding to the Cu_2Cyt/MXene interface, suggesting that electrons are further transferred from Cu_2Cyt complex to the underlying MXene substrate. These results collectively indicate a sequential ET pathway: electrons flow from C_2H_4 → Cu_2Cyt → MXene. The total transferred charge, quantified by the charge displacement curve (Fig. S11), is estimated to be 0.43 e^-.

Based on this charge redistribution, a sensing mechanism is proposed, as illustrated in Fig. 4c. In air, O (–COO^-) and H (–NH_2) of Cu_2Cyt form hydrogen bond with H (Ti–OH) and O (Ti–O terminal), respectively. Upon exposure to C_2H_4, the gas molecules are specifically captured by the Cu^+ active sites in Cu_2Cyt, forming coordination structure of Cu(I)-C_2H_4 (d-π conjugation). Subsequent electron donation from C_2H_4 initiates cascade electron transfer by two potential pathways (marked with p1 and p2) through the Cu_2Cyt complex into MXene. As a p-type semiconductor, MXene accepts these electrons into its vacant states, leading to an upward shift in the Fermi level, a reduced hole concentration, and an increase in electrical resistance. This resistance modulation serves as the measurable output signal for C_2H_4 detection. The hydrogen bonds can be evidenced by buleshift of Cu–O vibriation and redshift of Cu–N vibration (Fig. 4d). The former is caused by the increased electron density (O pulls electron from H of T–OH), while the latter is due to the decreased electron density (N loses electron to O of Ti–O terminal). Notably, Cu–S vibration disappears due to the interaction between MXene and Cu_2Cyt/MXene.

The interaction between MXene and Cu_2Cyt can be also demonstrated by time-dependent XRD patterns after mixing for 1, 5, 10, and 30 min (Fig. 4e). The characteristic peak centered around 6.3° can be assigned to the (200) plane of MXene[42], while that centered around 18.9° can be attributed to the (100) plane of Cu_2Cyt. The intensities of both peaks show an increase (high crystallinity) from 1 to 5 minutes and then a decrease (low crystallinity) from 10 to 30 min. The time-dependent crystallinity variations can be attributed to interconnect caused by surface interactions, which has been illustrated in Fig. 2. Similarly, the time-dependent FTIR spectroscopies also demonstrate the interactions between MXene and Cu_2Cyt (Fig. S12), because of the changing vibration modes caused by the formation of hydrogen bonds in the low frequency region along with time range of 1-30 min.

As shown in Fig. 4f, in-situ FTIR spectroscopies are further utilized to verify the dynamic recognition process of Cu_2Cyt to ethylene gas described in Fig. 4c. The characteristic peaks at 1888.7 cm^{-1} and 1912.7 cm^{-1} can be assigned to the combination and double vibrations of $=CH_2$ swing mode in Cu(I)-C_2H_4, respectively, while the characteristic peak at 949.8 cm^{-1} belongs to $=CH_2$ swing mode[43]. These characteristic peaks emerged exclusively upon ethylene exposure, and their intensity increased progressively from 1 to 3 minutes. This trend illustrates the gradual capture of ethylene molecules by the active Cu(I) sites in Cu_2Cyt. Notably, the peak intensity plateaued between 3 and 5 minutes, indicating that adsorption saturation was reached at approximately 3 minutes. This saturation time closely aligns with the response saturation time observed in the electrical measurements (~200 s), highlighting the effectiveness of in situ FTIR on illustrating the dynamic process of ethylene recognition.

The sensor was fabricated by drop-casting the Cu_2Cyt/MXene composite onto an IDE patterned on a flexible polyimide (PI) substrate. Optical microscopy images confirm the uniform coverage of the sensing film across the electrode gaps (Fig. S13). The performance was tested on the gas sensor testing system as shown in Supplementary Fig. S14. Current-voltage (I-V) measurements at different C_2H_4 concentrations reveal a linear relationship in the range of 0-2 V (Fig. S15), indicating that an ohmic contact is formed between the Cu_2Cyt/MXene layer and the IDEs[44]. To meet the low-power requirements of portable or outdoor applications, a low voltage of 0.1 V was selected for subsequent measurements. As shown in Fig. 4g, the Cu_2Cyt/MXene sensor exhibits a distinct and rapid response toward C_2H_4, featuring a response magnitude of 3.3%, an approximate 100% recovery rate, and response/recovery times (defined by 90% signal change) of 51/92 s, respectively. The response and recovery rate are defined by equation

(S1) and equation (S2), respectively, as presented in section S1 of Supplementary Information. In contrast, the pristine MXene sensor shows negligible response under the same conditions. Independent sensing tests of pure Cu_2Cyt were not feasible due to its low conductivity (1.01×10^{-4} $S\cdot cm^{-1}$), confirming that Cu_2Cyt alone cannot generate an electrical signal upon gas exposure. These results highlight the synergistic effect between Cu_2Cyt and MXene, wherein Cu_2Cyt serves as the selective recognition component, and MXene (3500 ± 500 $S\cdot cm^{-1}$) provides the conductive pathway for signal transduction via resistance change.

To optimize sensor performance, three parameters were systematically investigated: (i) the molar ratio of $CuCl_2$ to L-Cysteine during Cu_2Cyt synthesis, (ii) the molar ratio of Cu_2Cyt to MXene, and (iii) the drop-casting volume. Optimal sensing behavior was achieved at a synthesis ratio of 2:10 ($CuCl_2$: L-Cysteine), a mixing ratio of 50:5 (Cu_2Cyt : MXene), and a casting volume of 70 μL (Fig. S16). All subsequent measurements were conducted using electrodes prepared under these optimized conditions. To comprehensively explore alternative sensing materials, we also evaluated other common transition-metal complexes, including those of cobalt (Co), nickel (Ni), and zinc (Zn), under the same optimized conditions. As shown in Fig. S17, these complexes exhibit detectable responses to ethylene; however, their responses are significantly weaker than that of the Cu-based complex. This contrast further underscores the unique advantage of the copper-centered design, consistent with the highly efficient ethylene-binding mechanism evolved in plants.

In open systems, C_2H_4 released by plants typically ranges from 0.05 to 0.5 ppm, and may even drop to ppb level[45]. Based on this, nine representative C_2H_4 concentrations within this range were selected to evaluate the concentration-dependent response behavior of the optimized Cu_2Cyt/MXene sensor (Fig. 4h).

In the dynamic response curves, purple-shaded regions indicate exposure to C_2H_4 (introduced at 180 s), while the remaining intervals correspond to ambient air flushing. The sensors exhibits a clear increase in response with rising C_2H_4 concentrations. However, at higher concentrations, particularly above 1 ppm, the response increment becomes less pronounced, suggesting a sublinear trend toward saturation (Fig. 4i). To quantitatively describe this behavior, a response model integrating Langmuir gas adsorption theory with semiconductor principle[31,32,46], was developed, as shown in equation (1):

$$S(C) = \left(1 - \beta \times \frac{K \cdot C}{1 + K \cdot C}\right)^{-1} + \gamma \qquad (1)$$

where C is the C_2H_4 concentration, K is the adsorption equilibrium constant, $\beta = \alpha/P_0$, with α representing the hole depletion coefficient per adsorbed molecule, and P_0 the intrinsic carrier concentration of the sensing material. The parameter $\gamma = S(0) - 1$, where $S(0)$ is the baseline response. According to Langmuir theory, the response increases with concentration as more gas molecules are adsorbed, but approaches a plateau as active sites on the surface become saturated. The detailed derivation of this model is provided in Section S3 of Supplementary Information. Nonlinear regression fitting of the experimental data using equation (1) yields excellent agreement (red curve in Fig. 4i), with a determination coefficient $R^2 = 0.9909$. The fitted parameters were: $\beta = 0.88$, $K = 5.45$, and $S_0 = -0.02$. Notably, under the assumption that α and K remain constant, an increase in P_0 (*i.e.*, higher intrinsic hole density) would lead to a reduction in overall response amplitude, highlighting the importance of charge modulation in p-type semiconducting MXene.

At trace C_2H_4 concentrations, equation (1) can be simplified to a linearized equation (2) using a Taylor series expansion, as follows:

$$S(C) = \frac{\alpha \cdot K}{P_0} \times C \qquad (2)$$

Remarkably, even beyond the trace-level concentration regime, this linearized model provides an excellent fit to the experimental data in the 0.05-0.5 ppm range, with a coefficient of determination $R^2 = 0.9928$ (inset of Fig. 4i). The sensitivity (S), defined as the slope of the linear fit, is calculated to be 3.64% · ppm^{-1}. The limit of detection (LOD) was estimated using the standard formula $LOD=3\sigma/S$, where σ is standard deviation of the sensor tested for three times in air, yielding a remarkably low value of 1.07 ppb. This ultra-low LOD ensures reliable detection of C_2H_4 emissions at biologically relevant levels, such as those released by fruits and plants under postharvest or stress conditions. To comprehensively evaluate the practical viability of the Cu_2Cyt/MXene sensor, further performance tests were conducted, including assessments of selectivity, repeatability, reproducibility, signal stability under mechanical deformation, and environmental robustness, as detailed below.

To investigate how the growth evolution of Cu_2Cyt crystals influences sensing performance, we conducted time-series SEM characterization at key reaction intervals (5 min, 15 min, 30 min, 1 h, 2 h, and the final 3 h) and analyzed the corresponding particle-size distributions (Fig. 5). The size distributions were fitted using a Gaussian function, *i.e.* equation (3) below:

$$f(d) = A \times \exp\left[-\frac{(d-\bar{d})^2}{2\sigma^2}\right] \tag{3}$$

where d is the particle diameter, $f(d)$ is the probability density, $\bar{d}$ and σ are the fitted mean diameter and standard deviation, respectively, and A is a normalization constant. The time-dependent SEM images reveal a clear morphological progression from initial aggregates to well-defined microflowers. At the early stage (5 min), small flake-like units densely stack into compact, nascent flower-like structures with an average particle size of 11.86 ± 2.28 μm (Fig. 5a). As the reaction proceeds to 15–30 min, the primary nanosheets undergo self-assembly through oriented attachment and intermolecular interactions. The petals begin to spread, the layered stacking becomes more distinct, the flower contours sharpen, and the overall structure becomes looser (Fig. 5b, c). Correspondingly, the particle size increases to 12.18 ± 2.37 μm (15 min) and 13.46 ± 3.72 μm (30 min).

Between 60 and 120 min, the petal dimensions further increase and the packing density becomes higher, yielding average particle sizes of 15.78 ± 2.98 μm (60 min) and 16.61 ± 3.84 μm (120 min) (Fig. 5d, e). By 180 min, however, the microflower structure becomes severely damaged, showing a coexistence of large agglomerates and nanofibrous fragments, with the particle size expanding to 20.76 ± 5.24 μm (Fig. 5f). The standard deviation increases from 2.28 μm to 5.24 μm, reflecting a continuous evolution from primary aggregates to mature flower-like assemblies, followed by excessive collapse (Fig. S18a-f).

The particle-size evolution is consistent with an Ostwald ripening process, in which smaller crystallites dissolve and re-deposit onto larger ones over time[47], indicating that the synthesis is governed by thermodynamic control. Time-dependent XRD patterns confirm that the crystal structure remains unchanged throughout the growth process (Fig. S18g). The sensing response exhibits an initial increase followed by a decline, mirroring the morphological evolution (Fig. S18h). Because the improvement in response beyond 15 min was marginal, a reaction time of 15 min was selected for subsequent experiments.

To further elucidate how synthesis parameters steer this thermodynamic pathway, we systematically examined the effects of precursor concentration, reaction temperature, and pH (Figs. S19-S24). These results demonstrate that the morphology and particle size of the composite are strongly dictated by synthesis conditions, which in turn determine the sensing performance. Detailed analyses are provided in the Supplementary Information. Collectively, these insights offer a systematic foundation for the rational design of future multi-factor optimization strategies.

Selectivity is a vital parameter for practical gas sensors, especially in complex agricultural environments. The Cu_2Cyt/MXene sensor was evaluated against six common agricultural gases, including ammonia (NH_3), ethanol (EtOH), carbon dioxide (CO_2), nitrogen dioxide (NO_2), methane (CH_4), and isoprene (C_5H_8) (Fig. 6a). The sensor exhibits a significant response of 3.3% to 1 ppm C_2H_4, whereas the responses to non-olefin gases were negligible even at a higher concentration, with specific values as follows: 0.54% to 5 ppm EtOH, 0.48% to 5 ppm CO_2, 0.52% to 5 ppm NO_2, 0.49% to 5 ppm CH_4, and 0.51% to 50 ppm NH_3. Notably, the sensor shows a moderate response of 1.3% to 1 ppm isoprene, another olefin gas (Fig. S25). However, in practical agricultural environments, interference from isoprene is negligible, as plants typically emit isoprene at ambient concentrations that are several orders of magnitude lower than those of ethylene[48]. This high selectivity to ethylene gas is attributed to the Cu_2Cyt component, which highly mimics the biological evolved recognition mechanism of plant C_2H_4 receptor proteins.

The mechanical robustness of the Cu_2Cyt sensor was evaluated through graded bending tests, including four levels: flat (0°), slightly bent (~45°), half-folded (~90°), and fully folded (~180°). As shown in Fig. 6b, the sensor retained over 99% of its original response under the slight bending states, and maintained approximately 80% of its performance even under 180° folding. These results confirm the excellent mechanical robustness and flexibility of the sensor, supporting its application in wearable and flexible agricultural monitoring applications. Repeatability was evaluated through six consecutive exposure–recovery cycles at 1 ppm C_2H_4 (Fig. 6c). The response values remained stable with a relative standard deviation (RSD) below 0.069%, indicating excellent operational repeatability. Furthermore, device-to-device reproducibility was verified across eight independently fabricated Cu_2Cyt/MXene sensors. The measured responses showed minimal variation, with an RSD of 1.72% (Fig. 6d), demonstrating consistent fabrication quality and reliable sensing performance across batches.

The influence of temperature on sensor performance was investigated by exposing the Cu_2Cyt/MXene sensor to 1 ppm C_2H_4 at five temperatures ranging from 0 ℃ to 50 ℃ (Fig. 6e). The response increased with temperature from 0 to a maximum at approximately 20 ℃, after which it gradually declined with further temperature rise. According to Equation (2), assuming a constant hole depletion coefficient α, the sensor response is directly proportional to the adsorption equilibrium constant K and inversely proportional to the intrinsic carrier concentration P_0 of the MXene substrate. At lower temperatures (0-20 ℃), the increase in K dominates, likely due to enhanced gas adsorption, resulting in an overall rise in response. This suggests that adsorption-desorption kinetics play a leading role in this range. Instead, at elevated temperatures (20-50 ℃), the thermally induced increase in P_0 becomes dominant, which reduces the degree of charge modulation and thus suppresses the sensing signal. This competing relationship between adsorption affinity and semiconductor carrier dynamics results in a peak-shaped temperature–response curve, with an optimal operating temperature of approximately 20 ℃, where these effects are balanced.

The Cu_2Cyt/MXene sensor was evaluated under controlled relative humidity (RH) conditions ranging from 10% to 80% to assess the influence of environmental moisture on sensing performance. As shown in Fig. 6f, the sensor response exhibits a slightly increase below 50% RH (range I), and is followed by a gradual decline above 50% RH (range II). The underlying mechanism was investigated through theoretical calculations, which were provided at the bottom of Fig. 6f. In range I, water molecules form dynamic hydrogen bonds with the exposed Cu^+ of Cu_2Cyt, inducing conformational expansion that exposes previously shielded Cu^+ sites. This structural rearrangement enhanced the accessibility and adsorption efficiency for C_2H_4[49], as evidenced by a reduction in the adsorption Gibbs free energy to approximately 0.09 eV compared to the dry condition. Nevertheless, in range II, the presence of excessive water molecules leads to competitive adsorption on the Cu^+ active sites of Cu_2Cyt, which reduces the effective binding of C_2H_4[50], reflected by an increased adsorption Gibbs free energy (~0.12 eV higher than under dry conditions). In addition to humidity, molecular oxygen (O_2) also influences sensing performance (Fig. 6g). After eight days of ambient exposure, O_2 adsorbs onto the MXene surface and captures electrons to form superoxide radicals ($O_2^{\bullet -}$), which modulate the electronic properties of the sensing layer[51]. This electron withdrawal effect increasses the baseline carrier concentration P_0, thereby diminishing the signal modulation capacity upon C_2H_4 exposure[46]. In contrast, sensors stored in an inert argon atmosphere exhibited a much slower decline in response, confirming the detrimental role of O_2 adsorption. The bottom of Fig. 6g provides a diagrammatic explanation of this mechanism. To ensure long-term reliability in complex environments, it is recommended to incorporate hydrophobic surface modifications and antioxidant treatments, along with real-time environmental compensation algorithms, to maintain sensor stability and performance under fluctuating ambient conditions.

To evaluate its practical applicability, the Cu_2Cyt/MXene sensing electrode was integrated with a miniaturized U-disc electrochemical workstation capable of wireless Bluetooth connection to a tablet, enabling portable, real-time C_2H_4 detection and data visualization in field environments (Fig. 7a). The system architecture is illustrated in Supplementary Fig. S26. The first demonstration focused on monitoring C_2H_4 emissions from fruits. A sealed transparent acrylic chamber was used to test apples and bananas individually and in combination (Fig. 7b). The sensor exhibited a stronger response to bananas than to apples, and the highest response when both fruits were present. These results highlight the sensor's high sensitivity and its ability to distinguish C_2H_4 emissions profiles from different fruit sources. This observation is consistent with the physiological characteristics of the two fruits. Bananas are classified as climacteric fruits and exhibit a positive feedback loop in C_2H_4 biosynthesis, leading to a rapid, a self-amplifying ripening process[52,53]. In contrast, C_2H_4 release from apples is modulated by endogenous hormonal antagonism and restricted by the fruit's epidermal barrier, which suppresses immediate C_2H_4 surges to favor long-term storage[54,55]. To visually demonstrate the practical applicability of our sensors, the supplementary movies document the complete validation process (Supplementary Movies 1-3). These visual demonstrations, together with independent GC analysis confirming an ethylene concentration of 3.7 ppm in the fruit container (Fig. S27), provide strong scientific evidence that the Cu_2Cyt/MXene sensor delivers a reliable and accurate response under practical conditions.

In addition, a wearable sensing configuration was evaluated under open-environment conditions to simulate practical, on-fruit monitoring scenarios. The Cu_2Cyt/MXene electrode was affixed directly onto the surface of a mature apple, and continuous real-time monitoring of C_2H_4 emissions was conducted over a 24-hour period starting at 11:00 am. As shown in Fig. 7c, the C_2H_4 release exhibited a stepwise increase approximately every three hours. This trend is consistent with the enzymatic kinetics of C_2H_4 biosynthesis, where the activities of aminocyclopropane-1-carboxyllic acid (ACC) synthase and ACC oxidase peak during ripening, driving elevated C_2H_4 production and accelerated fruit maturation[56,57]. To further explore C_2H_4 dynamics at different physiological stages, apples at mature, senescent, and decayed stages were tested (Fig. 7d). The sensor response during the senescence was lower than that in the mature stage, whereas a slight increase was observed during decay. This pattern reflects the suppression of C_2H_4 production due to reduced respiration in senescence and a secondary rise during decay, likely caused by microbial activity and tissue degradation[58,59]. These results demonstrate the practical capability of the Cu_2Cyt/MXene sensor to sensitively track fruit ripeness, freshness, and spoilage in real time, offering a non-invasive and continuous monitoring tool for postharvest management.

Beyond agricultural applications, the sensor was also tested in a simulated industrial setting to detect C_2H_4 leakage. The device was attached over a small aperture on a C_2H_4 transmission pipeline using adhesive film. Upon exposure to 5 ppm of leaked C_2H_4 gas, a distinct resistance response was recorded (Fig. 7e), confirming the sensor's rapid response under leakage conditions. This wearable configuration provides a practical and cost-effective solution for real-time C_2H_4 leakage detection in industrial environments, enhancing safety monitoring within transport and storage infrastructure.

To benchmark the performance of the Cu_2Cyt/MXene sensor, a comparative analysis with previously reported C_2H_4 sensors was conducted, as summarized in Table 1. Unlike many reported sensors that rely on noble-metal catalysts such as Pd or Pt, the presented sensor is entirely noble-metal-free, significantly reducing material cost. In terms of detection capability, the sensor exhibits a wide linear range of 0.05-5 ppm and an ultra-low limit of detection (LOD) of 1.07 ppb, which is among the best reported for noble-metal-free sensors. Notably, the sensor operates effectively at room temperature (RT), in contrast to many oxide-based sensors (*e.g.*, porous ZnO, LIG-SnO_2) that require elevated working temperatures of 250-500 °C to achieve comparable performance.

The Cu_2Cyt/MXene sensor also demonstrates a rapid response/recovery time (51/92 s), outperforming several flexible sensors platforms such as SWCNT/PdNPs/Polystyrene (~500 s) and PdNPs-SWCNT@Cu-MOF-74 (200/50 s). To further accelerate the response speed, future work may focus on several key rate-limiting steps: (1) increasing the specific surface area of the sensing material to maximize active site exposure; (2) engineering a more porous sensing layer to promote rapid ethylene diffusion; (3) enhancing the catalytic activity of copper sites through doping or heterojunction design; (4) optimizing operational parameters such as temperature and bias voltage; and (5) fabricating electrodes with sub-micron gaps to shorten charge-transport pathways. These strategies provide a clear roadmap toward developing ultrafast sensors capable of real-time monitoring.

Compared with other MXene-based sensors incorporating noble-metal nanoparticles (*e.g.*, MXene@PdNP), the proposed sensor achieves superior sensitivity while maintaining excellent mechanical flexibility. It is noteworthy that the optimal bias voltage in this work — and in most reported studies-centers around 0.1 V, indicating a common operational window that effectively balances sensitivity and stability. This consistency further highlights our sensor's strong performance within a standard low-voltage framework. These advantages underscore the promise of the Cu_2Cyt/MXene sensor as a low-cost, high-performance, and wearable solution for real-time C_2H_4 monitoring in both agricultural and industrial applications.

Discussion

In summary, a biomimetic Cu_2Cyt complex, inspired from plant C_2H_4 receptor, has been synthesized via a facile method by the reaction between L-Cysteine and $CuCl_2$ in a certain ratio under alkaline condition. By mixing Cu_2Cyt with P-type MXene, a resistance-sensitive Cu_2Cyt/MXene composite was prepared successfully. The structures and properties of these materials were comprehensively characterized and analyzed by microscopy, spectroscopy, and theoretical calculation. The coordinated Cu^+ sites were confirmed to specifically recognize C_2H_4, triggering ET from Cu_2Cyt to MXene. The wearable sensors were fabricated by drop-casting the Cu_2Cyt/MXene composite onto IDEs patterned on a flexible PI substrate. Systematical performance tests demonstrate that the C_2H_4 sensors exhibit excellent response characteristics, good reproducibility and reversibility, as well as an ultralow LOD at room temperature. The concentration-dependent response behavior was elucidated by developing a model that integrates Langmuir gas adsorption theory with semiconductor principles, from which a linear relationship was derived within the trace concentration range.

It is worth noting that although the sensors are susceptible to environmental factors such as temperature, humidity and oxygen, the underlying interference mechanisms were systematically investigated and verified, providing a valuable foundation for designing more stable and reliable sensors under real-world conditions. Future studies will focus on exploring alternative p-type 2D materials — particularly stable reduced graphene oxide (rGO) and transition-metal dichalcogenides such as MoS_2 and WSe_2 — to further enhance the durability and practical deployment potential of this sensing architecture. Furthermore, on-site tests were conducted using the wearable sensors integrated with a Bluetooth device for wireless data collection, demonstrating the potential for real-time monitoring C_2H_4 released from fruits and detecting leaks in gas transport pipelines of chemical industries. This work highlights the practical applicability and scientific significance of the proposed bioinspired sensor platform, providing valuable guidance for developing real-time, low-cost, highly selective, room-temperature, and anti-interference C_2H_4 monitoring in both agricultural and industrial contexts.

Methods

Material characterization

The microstructure and element distribution of the samples were characterized by using scanning electron microscopy (QUANTA 250) with accessories of EDS and HRTEM (Tecnai G2 F20). XRD analyses were performed on a Rigaku B/Max-RB diffractometer. FTIR was measured on infrared spectrometer (Nexus 870). XPS was tested using Thermo ESCALAB 250XI. Raman spectra were conducted by Raman spectrometer with 532 nm light source (RTS Ultra). Nitrogen adsorption/desorption isotherms were tested on BET Surface Area Analyzer (Micromeritics Tristar 3000). EPR measurements were carried out on a Bruker EMX Plus spectrometer to analyze the electronic spin states of the samples. In situ FTIR spectra were recorded using a Nicolet iS50 FTIR spectrometer equipped with a custom-built in situ reaction cell to monitor the dynamic structural changes during the reaction process. Cross-sectional SEM observations were performed on the samples prepared by platinum deposition (for surface protection) followed by focused ion beam (FIB) milling with a gallium ion source (FEI Scios 2 HiVac) to precisely cut and fabricate the cross-sectional samples. GC was employed to determine the ethylene concentration in fruit boxes using an Agilent 7890A gas chromatograph.

Manufacture procedures of sensors

Synthesis of Cu_2Cyt complex. NaOH (120 mg, 3 mmol) and L-Cysteine (484.64 mg, 4 mmol) were dissolved in 3 mL of deionized water and thoroughly mixed. The reaction was conducted under ambient air with the mixture maintained at 500 rpm under magnetic stirring. Subsequently, 3 mL of $CuCl_2$ solution (107.56 mg, 0.8 mmol) was slowly added dropwise to the mixture under continuous stirring. The reaction was allowed to proceed for 15 minutes to facilitate the formation of Cu_2Cyt nanosheets. Upon completion, the resulting precipitate was collected by centrifugation at 10270 x g for 10 minutes, and washed sequentially with deionized water and ethanol to remove unreacted residues. The purified Cu_2Cyt product was then redispersed in 15 mL of absolute ethanol and stored at 4 °C for further use. In addition, key parameters, including precursor concentrations, reaction time, reaction temperature, pH values (controlled by NaOH dosage), and stirring conditions are summarized in Table S1.

Preparation of Cu_2Cyt/MXene composite. Cu_2Cyt/MXene composite was obtained by mixing 1 mL of the synthesized Cu_2Cyt solution and 100 μL of $Ti_3C_2T_X$ dispersion (5 mg/mL), followed by ultrasonication for 10 minutes to ensure uniform blending. $Ti_3C_2T_x$ MXene monolayer dispersion (product code: XFK04-1; Concentration: 5 mg/mL) used in this study was commercially acquired from XFNANO Materials Tech Co., Ltd., Nanjing, Jiangsu, China.

Fabrication of sensors with Cu_2Cyt/MXene composite. 50 μL of Cu_2Cyt/MXene solution was droped onto gold interdigitated electrodes with a polyimide substrate. The electrodes were dried at 60 ℃ for 30 minutes in a drying oven to complete the sensor fabrication. The interdigitated electrodes are composed of copper and gold layers with thicknesses of 18 μm and 1 μm, respectively. The available region of interdigitated electrodes is 12 mm × 10 mm, which contains 12 pairs of interdigitated fingers with an inter-finger spacing of 200 μm.

Data availability

All data generated in this study are provided in the Supplementary Information/Source Data file. Source data are provided with this paper.

References

1. Huang, J., Zhao, X., Bürger, M., Chory, J. & Wang, X. The role of ethylene in plant temperature stress response. *Plant Sci.* **28**, 808-824 (2023).

2. Schwab, S.T., Baur, M., Nelson, T. F., & Mecking, S. Synthesis and deconstruction of polyethylene-type materials. *Chem. Rev.* **124**, 2327-2351 (2024).

3. Ma, X., Liu, Y., Liu, H. & Gu, K. Ethylene Leak Detection Based on Infrared Imaging: A Benchmark. In: *2023 IEEE 11th International Conference on Information, Commun. and Netw. (ICICN)*) (2023).

4. Arcudi, F., Đorđević, L., Schweitzer, N., Stupp, S. I., & Weiss, E. A. Selective visible-light photocatalysis of acetylene to ethylene using a cobalt molecular catalyst and water as a proton source. *Nat. chem.* **9**, 1007-1012 (2022).

5. Wu, M.*, et al.* A biocompatible ruthenium-based composite fluorescent probe using bovine serum albumin as a scaffold for ethylene gas detection and its fluorescence imaging in plant tissues. *Chem. Eng. J.* **435**, 135045 (2022)

6. Chen, K.*, et al*. Photoacoustic trace gas detection of ethylene in high-concentration methane background based on dual light sources and fiber-optic microphone. *Sens. Actuat. B: Chem.* **310**, 127825 (2020)

7. Xu, J. Y., Fan, X. X., Xu, K. C., Wu, K. D., Liao, H. L. & Zhang, C. Ultrasensitive Chemiresistive Gas Sensors Based on Dual-Mesoporous Zinc Stannate Composites for Room Temperature Rice Quality Monitoring. *Nano-Micro Lett.* **17**, 359-373 (2025).

8. Zhao, X. F.*, et al.* Titanium nitride sensor for selective NO_2 detection. *Nat. Commun.* **16**, 182 (2025).

9. Wang, L. P*., et al.* The detection of ethylene using porous ZnO nanosheets: utility in the determination of fruit ripeness. *New J.Chem.* **43**, 3619-3624 (2019).

10. Zevenbergen, M. A. G., Wouters, D., Dam, V. A. T., Brongersma, S. H. & Crego-Calama, M. Electrochemical Sensing of Ethylene Employing a Thin Ionic-Liquid Layer. *Anal. Chem.* **83**, 6300-6307 (2011).

11. Tolentino, M. A. K. P., Albano, D. R. B. & Sevilla, F. B. Piezoelectric sensor for ethylene based on silver(I)/polymer composite. *Sens. Actuat. B: Chem.* **254**, 299-306 (2018).

12. Caprioli, F., & Quercia, L. Ethylene detection methods in post-harvest technology: A review. *Sens. Actuat. B: Chem.*, **203**, 187-196 (2014).

13. Jia, X*., et al.* Building Feedback-Regulation System Through Atomic Design for Highly Active SO2 Sensing. *Nano-Micro Lett.* **16**, 136 (2024).

14. Bulemo, P. M*., et al.* Selectivity in Chemiresistive Gas Sensors: Strategies and Challenges. *Chem. Rev.* **125**, 4111-4183 (2025).

15. Yan, H. L*., et al.* A flexible and wearable paper-based chemiresistive sensor modified with SWCNTs-PdNPs-polystyrene microspheres composite for the sensitive detection of ethylene gas: A new method for the determination of fruit ripeness and corruption. *Anal. Chim. Acta* **1239**, 340724 (2023).

16. Wu, Z. X*., et al.* A Self-Powered, Rechargeable, and Wearable Hydrogel Patch for Wireless Gas Detection with Extraordinary Performance. *Adv. Funct. Mater.* **33**, 2300046 (2023).

17. Zong, B. Y., Wu, S. F., Yang, Y. H., Li, Q. J., Tao, T. & Mao, S. Smart Gas Sensors: Recent Developments and Future Prospective. *Nano-Micro Lett.* **17**, 55-86 (2025).

18. Chen, R. P.*, et al.* Applications of MXenes in wearable sensing: Advances, challenges, and prospects. *Mater. Today* **75**, 359-385 (2024).

19. Fong, D., Luo, S. X. L., Andre, R. S. & Swager, T. M. Trace Ethylene Sensing via Wacker Oxidation. *ACS Central Sci.* **6**, 507-512 (2020).

20. Li, B., Li, M., Meng, F. & Liu, J. Highly sensitive ethylene sensors using Pd nanoparticles and rGO modified flower-like hierarchical porous α-Fe_2O_3. *Sens. Actuat. B: Chem.* **290**, 396-405 (2019).

21. Ishihara, S.*, et al.* Cascade Reaction-Based Chemiresistive Array for Ethylene Sensing. *ACS Sens.* **5**, 1405-1410 (2020).

22. Jeong, S. Y.*, et al.* A New Strategy for Detecting Plant Hormone Ethylene Using Oxide Semiconductor Chemiresistors: Exceptional Gas Selectivity and Response Tailored by Nanoscale Cr_2O_3 Catalytic Overlayer. *Adv. Sci.* **7**, 1903093 (2020).

23. Fu, W., Dijkman, T. F., Lima, L. M. C., Jiang, F., Schneider, G. F. & Bouwman, E. Ultrasensitive Ethene Detector Based on a Graphene–Copper(I) Hybrid Material. *Nano Lett.* **17**, 7980-7988 (2017).

24. Ren, X. N., Zhang, X. W., Cao, X. Z. & Wang, Q. F. Efficient electrochemical reduction of carbon dioxide into ethylene boosted by copper vacancies on stepped cuprous oxide. *J. CO_2 Util.* **38**, 125-131 (2020).

25. Zeng, L. Z.*, et al.* Multiple Cuprous Centers Supported on a Titanium-Based Metal-Organic Framework Catalyze CO_2 Hydrogenation to Ethylene. *ACS Catal.* **11**, 11696-11705 (2021).

26. Noonikara Poyil, A.*, et al.* A Molecular Compound for Highly Selective Purification of Ethylene. *Angew. Chem. Int. Ed.* **60**, 27184-27188 (2021).

27. Ma, Q. & Dong, C. H. Regulatory functions and molecular mechanisms of ethylene receptors and receptor-associated proteins in higher plants. *Plant Growth Regul.* **93**, 39-52 (2021).

28. Binder, B. M. Ethylene signaling in plants. *J. Biol. Chem.* **295**, 7710-7725 (2020).

29. Rigo, A., Corazza, A., Luisa, M., Rossetto, M., Ugolini, R. & Scarpa, M. Interaction of copper with cysteine: stability of cuprous complexes and catalytic role of cupric ions in anaerobic thiol oxidation. *J. Inorg. Biochem.* **98**, 1495-1501 (2004).

30. Ma, B. J.*, et al.* Self-Assembled Copper Amino Acid Nanoparticles for in Situ Glutathione "AND" H_2O_2 Sequentially Triggered Chemodynamic Therapy. *J. Am. Chem. Soc.* **141**, 849-857 (2019).

31. Gomri, S., Seguin, J. L., Guerin, J. & Aguir, K. Adsorption–desorption noise in gas sensors: Modelling using Langmuir and Wolkenstein models for adsorption. *Sens. Actuat. B: Chem.* **114**, 451-459 (2006).

32. Zhang, X. W., Zhang, J. P. & Chen, X. M. Molecule-Based Crystalline Adsorbents: Advancing Adsorption Theory and Storage/Separation Applications. *Acc. Mater. Res.* **6**, 259-273 (2025).

33. Frisch, M.*, et al.* Gaussian 16 Revision C. 01, 2016. *Gaussian Inc Wallingford CT* **1**, 572 (2016).

34. Song, M., Li, W. W., Zhang, X. L., Liu, J. X., Li, K. & Zhang HZ. Structural Stability of L-Cystine under Extreme Conditions. *ACS Earth. Space Chem.* **5**, 1525-1534 (2021).

35. Shearer J., Neurock M. & Mavrikakis M. Scaling relationships and theory for vibrational frequencies of adsorbates on transition metal surfaces. *Nat. Catal.* **4**, 363–370 (2021).

36. Saleem, S., *et al.* Enhancement in structural, morphological, and optical properties of copper oxide for optoelectronic device applications. *Nanotechnol. Rev.* **11**, 2827-2838 (2022).

37. Yin, Z., *et al.* Flotation separation of molybdenite from chalcopyrite using an environmentally-efficient depressant L-cysteine and its adsoption mechanism. *Miner. Eng.* **156**, 106438 (2020).

38. Luo, Y., *et al.* Decoding the redox behaviour of copper in Ullmann-type coupling reactions. *Nature*, **646**, 1105–1113 (2025).

39. Bain, D., *et al.* Solvent-Induced Aggregation of Self-Assembled Copper-Cysteine Nanoparticles Reacted with Glutathione: Enhancing Linear and Nonlinear Optical Properties. *Langmuir* **39**, 16554-16561 (2023).

40. Zhao, B., *et al.* In situ self-heterogenization of Cu_2S/CuS nanostructures with modulated d band centers for promoting photocatalytic degradation and hydrogen evolution performances. *Mater. Today Nano* **23**, 100362 (2023).

41. Yang, T., Chen, Z. W., Yue, X. Z., Liu, Q. C., Yi, S. S. & Zhu Y. F. Interfacial Charge Transfer Bridge Prolongs Carrier Recombination Lifetimes of CoFe Metal-Thiolate Framework/Hematite Photoanode for Water Oxidation. *Adv. Funct. Mater.* **34**, 2313767 (2024).

42. Cai Y., *et al.* $Ti_3C_2T_x$ MXene/urchin-like PANI hollow nanosphere composite for high performance flexible ammonia gas sensor. *Anal. Chim. Acta* **1225**, 340256 (2022).

43. Huang, Y. Y. Ethylene complexes in copper (I) and silver (I) Y zeolites. *J. catal.* **61**, 461-476 (1980).

44. Chen, X.*, et al.* Ultratrace antibiotic sensing using aptamer/graphene-based field-effect transistors. *Biosens. Bioelectron.* **126**, 664-671 (2019).

45. Keller, N., Ducamp, M., Robert, D. & Keller, V.. Ethylene Removal and Fresh Product Storage: A Challenge at the Frontiers of Chemistry. Toward an Approach by Photocatalytic Oxidation. *Chem. Rev.* **113**, 5029-5070 (2013).

46. Kumar, A., Kumar, M., Kumar, R., Singh, R., Prasad, B. & Kumar, D. Numerical model for the chemical adsorption of oxygen and reducing gas molecules in presence of humidity on the surface of semiconductor metal oxide for gas sensors applications. *Mat. Sci. Semicon. Proc.* **90**, 236-244 (2019).

47. Huang, Z., *et al*. A general patterning approach by manipulating the evolution of two-dimensional liquid foams. *Nat. commun.* **8**, 14110 (2017).

48. Jia, Y., Qiao, L., Xie, W. & Li, L. Sptial-temporal characteristics of ambient isoprene and monoterpene and their ozone and secondary organic aerosol formation potential in China. *Environ. Rev.* **32**, 203-213 (2024).

49. Wang, X. Y.*, et al.* Enhancing the chemical stability of MXene through synergy of hydrogen bond and coordination bond in aqueous solution. *Small Methods* **7**, 2201694 (2023).

50. Liu, B., Younis, S. A. & Kim, K. H. The dynamic competition in adsorption between gaseous benzene and moisture on metal-organic frameworks across their varying concentration levels. *Chem. Eng. J.* **421**, 127813 (2021).

51. Samaniego, J. I., Wang, X., Andersson, L., Malaspina, D., Ergun, R.E. & Horányi, M. J. Investigation of coatings for Langmuir probes in an oxygen-rich space environment. *J. Geophys. Res. Space Physics* **123**, 6054-6064 (2018).

52. Jin, Z. Q., *et al.* Identification of genes differentially expressed at the onset of the ethylene climacteric in banana. *Postharvest Biol. Tec.* **52**, 307-309 (2009).

53. Tipu, M. M., & Sherif, S. M. Ethylene and its crosstalk with hormonal pathways in fruit ripening: mechanisms, modulation, and commercial exploitation. *Front. Plant Sci.* **15**, 1475496 (2024).

54. Johnston, J. W., Gunaseelan, K., Pidakala, P., Wang, M. & Schaffer, R. J. Co-ordination of early and late ripening events in apples is regulated through differential sensitivities to ethylene. *J. Exp. Bot.* **60**, 2689-2699 (2009).

55. Li, T., *et al.* Phosphorylation of MdCYTOKININ RESPONSE FACTOR4 suppresses ethylene biosynthesis during apple fruit ripening. *Plant Physiol.* **191**, 694-714 (2023).

56. Esser, B., Schnorr, J. M. & Swager, T. M. Selective Detection of Ethylene Gas Using Carbon Nanotube-based Devices: Utility in Determination of Fruit Ripeness. *Angew. Chem. Int. Ed.* **51**, 5752-5756 (2012).

57. Shin, D. U., *et al.* Potassium permanganate-based ethylene gas indicator of kiwifruit ripeness. *Postharvest Biol. Tec.* **200**, 112330 (2023).

58. Van de Poel, B., Smet, D., & Van Der Straeten, D. Ethylene and hormonal cross talk in vegetative growth and development. *Plant Physiol.* **169**, 61-72 (2015).

59. Keller, N., Ducamp, M. N., Robert, D. & Keller, V. Ethylene removal and fresh product storage: a challenge at the frontiers of chemistry. Toward an approach by photocatalytic oxidation. *Chem. Rev.* **113**, 5029-5070 (2013).

60. Yang, J. W.*, et al.* A self-heating gas sensor for online monitoring of endogenous ethylene of post-harvest cut chrysanthemums. *Sens. Actuat. B: Chem.* **417**, 136094 (2024).

61. Chen, W. Y. Y.*, et al.* Selective Detection of Ethylene by MoS_2-Carbon Nanotube Networks Coated with Cu(I)-Pincer Complexes. *ACS Sens.* **5**, 1699-1706 (2020).

62. Li, X.*, et al.* Room temperature agricultural ethylene detection by freestanding three-dimensional porous-ZnO/carbon nanofibers. *Sens. Actuat. B: Chem.* **398**, 134737 (2024).

63. Li, X.*, et al.* All-MXene-Printed RF Resonators as Wireless Plant Wearable Sensors for In Situ Ethylene Detection. *Small* **19**, 2207889 (2023).

64. Yan, H., Wang, J., Shi, N., Han, Y., Zhang, S. & Zhao, G. A flexible and wearable chemiresistive ethylene gas sensor modified with PdNPs-SWCNTs@Cu-MOF-74 nanocomposite: a targeted strategy for the dynamic monitoring of fruit freshness. *Chem. Eng. J.* **488**, 151142 (2024).

Acknowledgements

This work was financially supported by the Henan Province Science and Technology Research (Joint Fund) Project (No. 242103810027) (J. W.).

Author contributions Statement

J. H., Z. Z. and J. W. were responsible for supervising the entire project and revising the manuscript. J. W. conceived the study, designed the experiments, provided the financial support, wrote and edited the manuscript. L. X. completed most of the experiments and wrote the first manuscript. B. Z. and H. X. conducted density functional theory calculations, and B. Z. participated in the writing and formatting of the manuscripts. B. T. and Z. Q. Z. carried out characterization tests and assisted in analyzing the characterization data. Y. L., X. C., H. Z. and L. L. assisted in conducting experiments and analyzing data. L. X and B. Z. made the same contribution to this work.

Competing interest Statement

The authors declare no conflict of interest.

Tables

Table 1. Comparison of key parameters of ethylene sensors between this work and recently reported studies.

Material	Noble-metal catalysis	Linear range (ppm)	LOD (ppb)	Texture	Temp. (°C)	Bias voltage (V)	Response/ recovery time (s)	Refs.
LIG/SnO_2	No	0.05-100	1.65	Rigid	250	5.5*	~140/210	60
$Pd/V_2O_5/TiO_2$	Yes	1-100	200	Rigid	40	0.1	~340/550	21
Porous ZnO	No	10-2000	5000	Rigid	500	-	~8/20	9
Pd/rGO/α-Fe_2O_3	Yes	0.01-1000	-	-	250	-	~18/50	20
Pd/Nitrite-4-Pyridyl /SWCNT	Yes	0.5-50	15	Rigid	RT	-	~60/240	19

2-MoS_2/SCNT	No	0.1-1	100	Rigid	RT	0.1	~102/215	61
ZnO/CNF	No	10-100	-	Rigid	RT	-	~133/169	62
MXene@PdNPs	Yes	0.5-20	84	Flexible	RT	-	~92/113	63
SWCNT/PdNPs/ Polystyrene	Yes	0.1-100	-	Flexible	RT	0.1	~500/-	15
PdNPs-SWCNT@Cu-MOF-74	Yes	0.1-100	31	Flexible	RT	0.1	~200/50	64
Cu_2Cyt/MXene	No	0.05-5	1.07	Flexible	RT	0.1	~51/92	This work

* The higher bias voltage is due to the fact that the sensor requires heating.

Figure Legends/Captions (for main text figures)

Fig. 1 Schematic illustration of the biomimetic C_2H_4 recognition mechanism. (**a**) C_2H_4 perception model of plant receptor and corresponding intracellular signaling pathway; (**b**) Bioinspired C_2H_4 sensing strategy based on a synthesized Cu_2Cyt complex that mimics the Cu^+-coordinated active site of the plant receptor. Upon C_2H_4 binding, the sulfur bridged Cu(I) center enables specific recognition and triggers electron transfer within the Cu_2Cyt/MXene heterostructure, resulting in resistance-related response.

Fig. 2 Structural characterization of Cu_2Cyt and Cu_2Cyt/MXene composite. (**a-b**) SEM images of the peony-like morphology of pure Cu_2Cyt; (**c**) SEM image of Cu_2Cyt with corresponding elemental mapping of C, N, Cu, O, and S; (**d-e**) SEM images of the Cu_2Cyt/MXene composite; (**f**) Elemental mapping of Ti, N, Cu, O, and S in the Cu_2Cyt/MXene composite; (**g-h**) SEM images of the cross-sectional view of Cu_2Cyt/MXene, the region with dotted line corresponds to Pt protective layer, which serves to ensure cutting completeness; (**i**) Elemental mapping of N, Cu, O, S, and Ti in the cross-sectional area; (**j**) High-magnification SEM image of Cu_2Cyt petals; (**k**) HR-TEM image of Cu_2Cyt; Among them, the above electron microscope images were reproduced in 3 independent synthesis batches. (**l**) XRD patterns of commercial L-Cysteine and synthesized Cu_2Cyt (using Cu Kα radiation). Source data are provided as a Source Data file.

Fig. 3 Properties analysis of related materials. (**a**) Reaction equation for Cu_2Cyt synthesis, along with the optimized structures of reactants and products, and the Gibbs free energy; (**b**) Raman spectra of L-Cysteine and Cu_2Cyt; (**c**) FTIR spectra of L-Cystine and Cu_2Cyt; High-resolution XPS spectrum of Cu 2p (**d**) and S 2p (**e**) for Cu_2Cyt; inset in (**d**) shows optical images of Cu_2Cyt before and after washing; (**f**) High-resolution C1s XPS spectrum of Cu_2Cyt/MXene composite. Source data are provided as a Source Data file.

Fig. 4 The C_2H_4 sensing mechanism and performance of Cu_2Cyt/MXene. (**a**) DFT-calculated binding energy of Cu_2Cyt with C_2H_4 at different Cu^+ coordination sites. (**b**) Differential charge density distribution for C_2H_4 adsorption on Cu_2Cyt/MXene, and charge variation along the z-axis; (**c**) Schematic illustration of the C_2H_4 sensing mechanism based on ET from Cu_2Cyt to MXene; (**d**) FTIR spectra of MXene, Cu_2Cyt and Cu_2Cyt/MXene; (**e**) Time-dependent XRD patterns of Cu_2Cyt/MXene with different mixing times ranging from 1 to 30 min; (**f**) In-situ FTIR spectra of Cu_2Cyt/MXene during ethylene exposure. (**g**) Response/recovery curves of pure MXene and Cu_2Cyt/MXene composite toward 1 ppm C_2H_4 at room temperature; (**h**) Dynamic response of Cu_2Cyt/MXene at 0.05-5 ppm; (**i**) Nonlinear fitting of the response-concentration relationship based on a Langmuir–semiconductor hybrid model, inset: linear fitting in the trace range (0.05-0.5 ppm). Source data are provided as a Source Data file.

Fig. 5 SEM images and corresponding particle size distribution statistics of Cu_2Cyt at different reaction times: (**a**) 5 min, (**b**) 15 min, (**c**) 30 min, (**d**) 60 min, (**e**) 120 min, and (**f**) 180 min. Among them, the above SEM images morphology were reproduced in 2 independent synthesis batches. The bottom panels present the particle size distribution histograms and Gaussian fitting curves. The numbers in the bottom panels represent $\bar{d}\pm\sigma$. Source data are provided as a Source Data file.

Fig. 6 Performance and environmental stability tests of Cu_2Cyt/MXene sensors toward 1 ppm C_2H_4 at room temperature. (**a**) Selectivity against common interfering gases; (**b**) Mechanical flexibility under different bending states; (**c**) Repeatability over six cycles; (**d**) Reproducibility across eight independently fabricated sensors. (**e**) Response behavior under different temperatures; (**f**) Response behavior under varying relative humidity, the inset shows its influence mechanism calculated by DFT; (**g**) Effect of oxygen exposure on response, with the inset depicting the proposed mechanism of oxygen-induced interference. Source data are provided as a Source Data file.

Fig. 7 Practical demonstrations of the Cu_2Cyt/MXene sensor. (**a**) Schematic of portable C_2H_4 detection using a Bluetooth-integrated three-electrode wearable device, the reference and counter electrode clips are short-circuited and connected to one IDE pad, while the working electrode clip is connected to the other pad, enabling operation in a two-electrode mode; (**b**) Real-time response to C_2H_4 emitted from bananas, apples, and their mixture in a sealed chamber; (**c**) Continuous monitoring of C_2H_4 released from an apple over 24 h in an open environment; (**d**) C_2H_4 detection at maturity, senescence, and decay periods of apple; (**e**) Real-time monitoring of C_2H_4 leakage from a simulated transport pipeline. Source data are provided as a Source Data file.

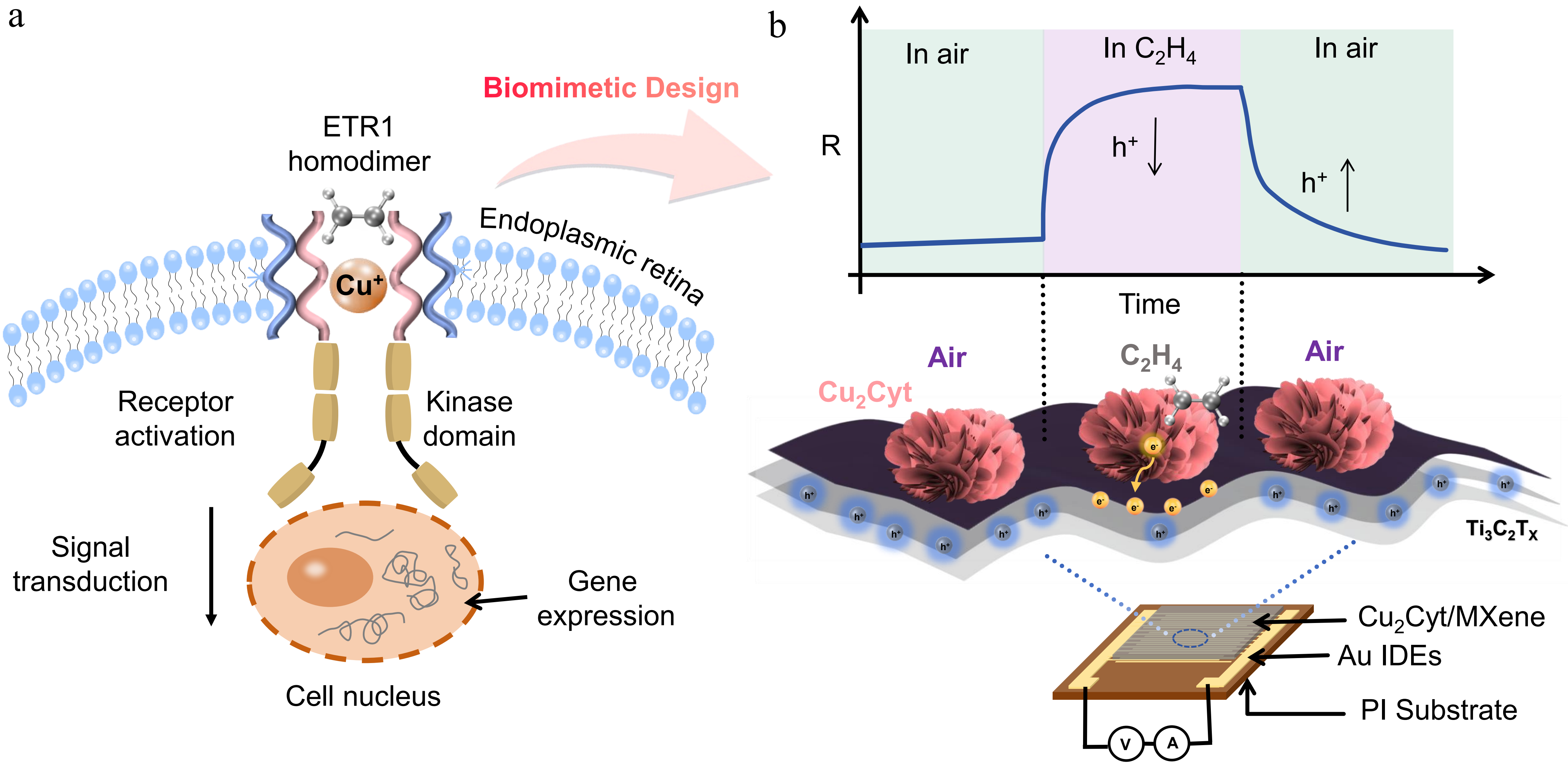
a
Biomimetic Design
ETR1 homodimer
Endoplasmic retina
Cu$^+$
Receptor activation
Kinase domain
Signal transduction
Gene expression
Cell nucleus
b
R
In air
In C_2H_4
In air
h$^+$ ↓
h$^+$ ↑
Time
Air
C_2H_4
Air
Cu_2Cyt
e$^-$
h$^+$
$Ti_3C_2T_x$
Cu_2Cyt/MXene
Au IDEs
PI Substrate
V
A

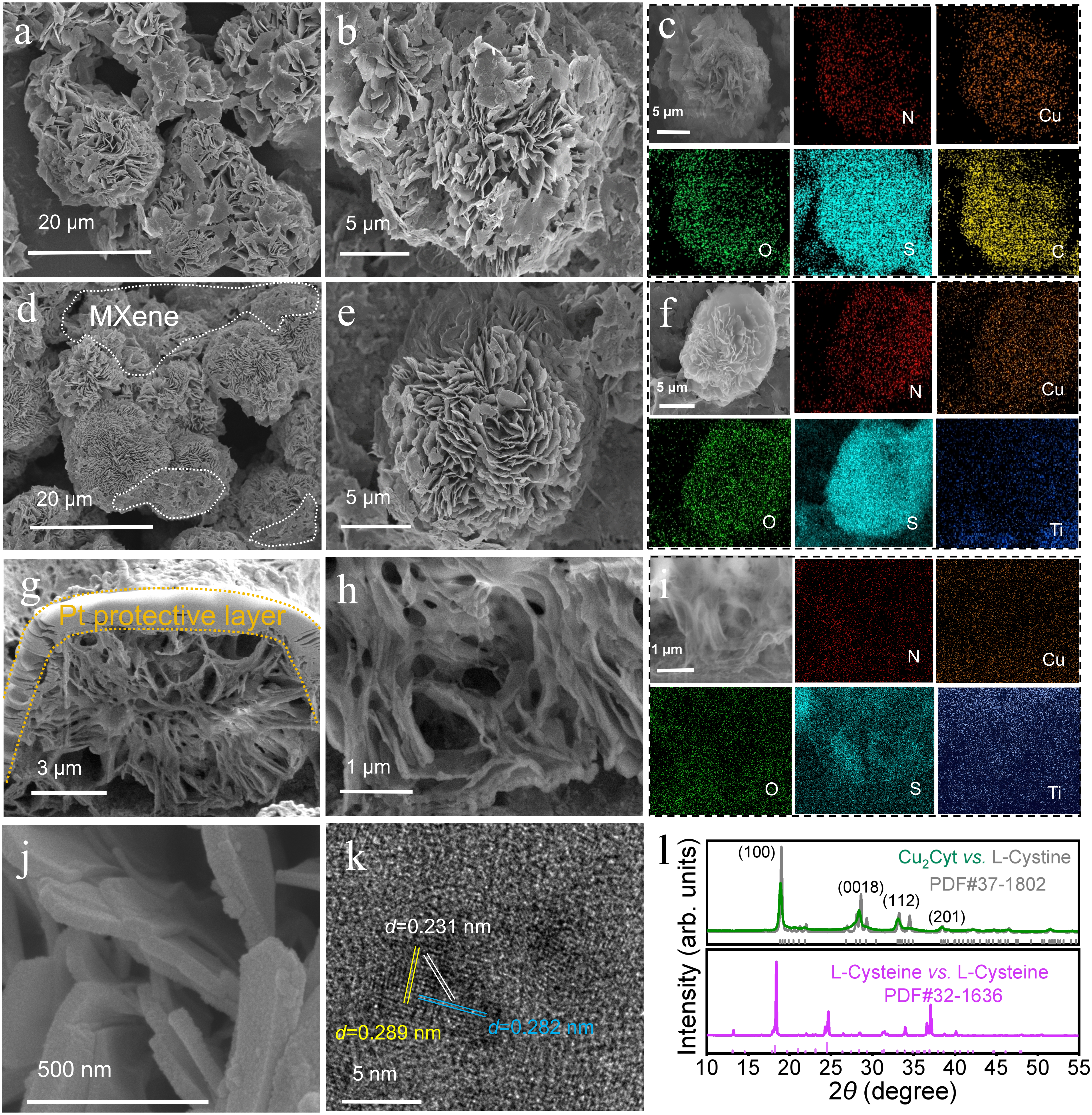
a
20 μm
b
5 μm
c
5 μm
N
Cu
O
S
C
d
MXene
20 μm
e
5 μm
f
5 μm
N
Cu
O
S
Ti
g
Pt protective layer
3 μm
h
1 μm
i
1 μm
N
Cu
O
S
Ti
j
500 nm
k
d=0.231 nm
d=0.289 nm
d=0.282 nm
5 nm
l
(100)
(0018)
(112)
(201)
Cu_2Cyt vs. L-Cystine
PDF#37-1802
L-Cysteine vs. L-Cysteine
PDF#32-1636
Intensity (arb. units)
10
15
20
25
30
35
40
45
50
55
2θ (degree)

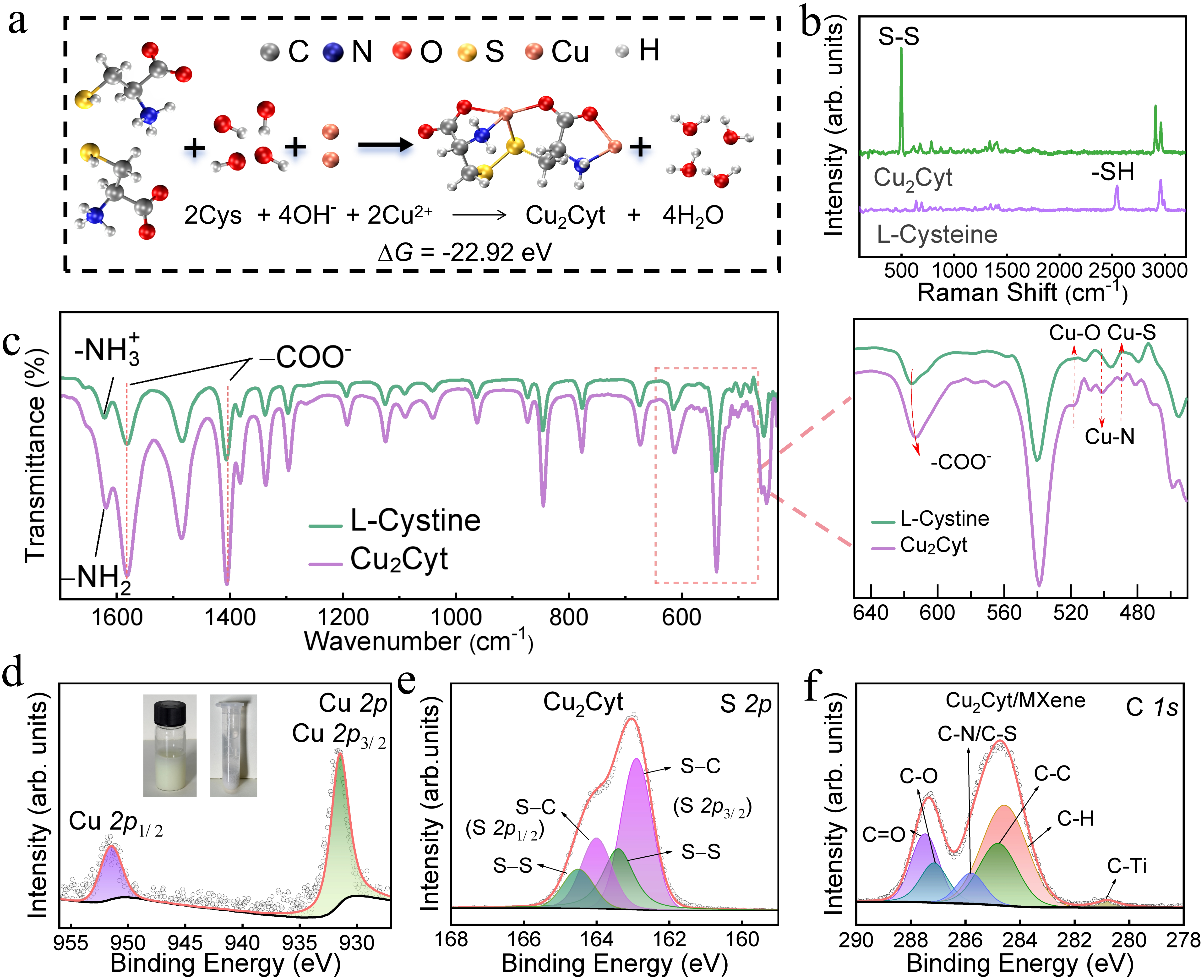
a
C
N
O
S
Cu
H
2Cys + 4OH⁻ + 2Cu²⁺ ⟶ Cu₂Cyt + 4H₂O
ΔG = -22.92 eV
b
S-S
Cu₂Cyt
-SH
L-Cysteine
Intensity (arb. units)
500 1000 1500 2000 2500 3000
Raman Shift (cm⁻¹)
c
-NH₃⁺
–COO⁻
–NH₂
L-Cystine
Cu₂Cyt
Transmittance (%)
1600 1400 1200 1000 800 600
Wavenumber (cm⁻¹)
Cu-O Cu-S
Cu-N
-COO⁻
L-Cystine
Cu₂Cyt
640 600 560 520 480
d
Cu 2p
Cu 2p3/2
Cu 2p1/2
Intensity (arb. units)
955 950 945 940 935 930
Binding Energy (eV)
e
Cu₂Cyt
S 2p
S–C
(S 2p3/2)
S–C
(S 2p1/2)
S–S
S–S
Intensity (arb.units)
168 166 164 162 160
Binding Energy (eV)
f
Cu₂Cyt/MXene
C 1s
C-N/C-S
C-O
C-C
C-H
C=O
C-Ti
Intensity (arb. units)
290 288 286 284 282 280 278
Binding Energy (eV)

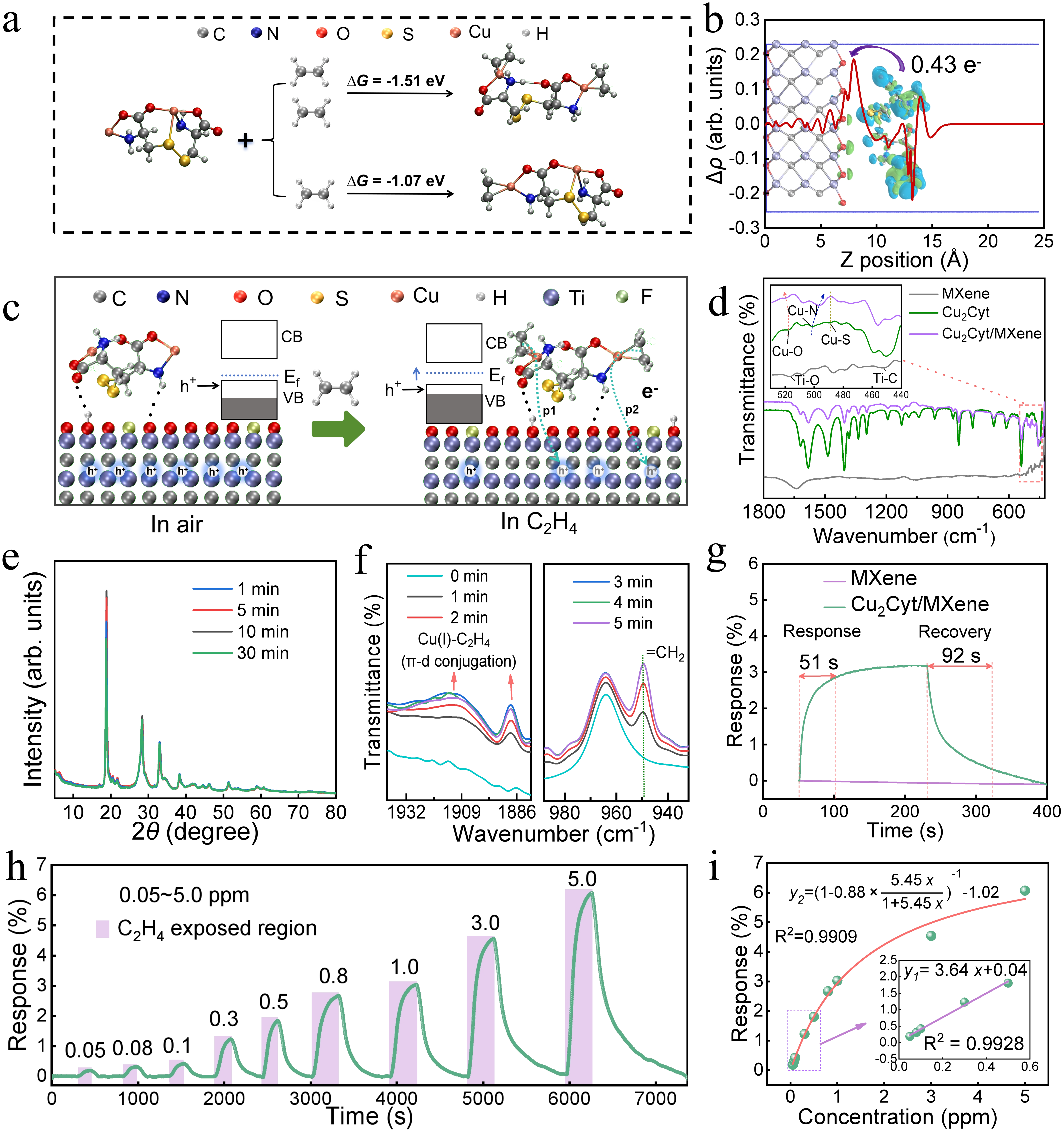
a
C N O S Cu H
ΔG = -1.51 eV
ΔG = -1.07 eV
b
0.43 e-
Δρ (arb. units)
Z position (Å)
c
C N O S Cu H Ti F
CB
Ef
VB
h+
p1
p2
e-
In air
In C2H4
d
MXene
Cu2Cyt
Cu2Cyt/MXene
Cu-N
Cu-S
Cu-O
Ti-O
Ti-C
Transmittance (%)
Wavenumber (cm-1)
e
1 min
5 min
10 min
30 min
Intensity (arb. units)
2θ (degree)
f
0 min
1 min
2 min
Cu(I)-C2H4
(π-d conjugation)
3 min
4 min
5 min
=CH2
Transmittance (%)
Wavenumber (cm-1)
g
MXene
Cu2Cyt/MXene
Response
Recovery
51 s
92 s
Response (%)
Time (s)
h
0.05~5.0 ppm
C2H4 exposed region
0.05 0.08 0.1 0.3 0.5 0.8 1.0 3.0 5.0
Response (%)
Time (s)
i
y2=(1-0.88 × 5.45 x / (1+5.45 x))^-1 -1.02
R2=0.9909
y1= 3.64 x+0.04
R2 = 0.9928
Response (%)
Concentration (ppm)

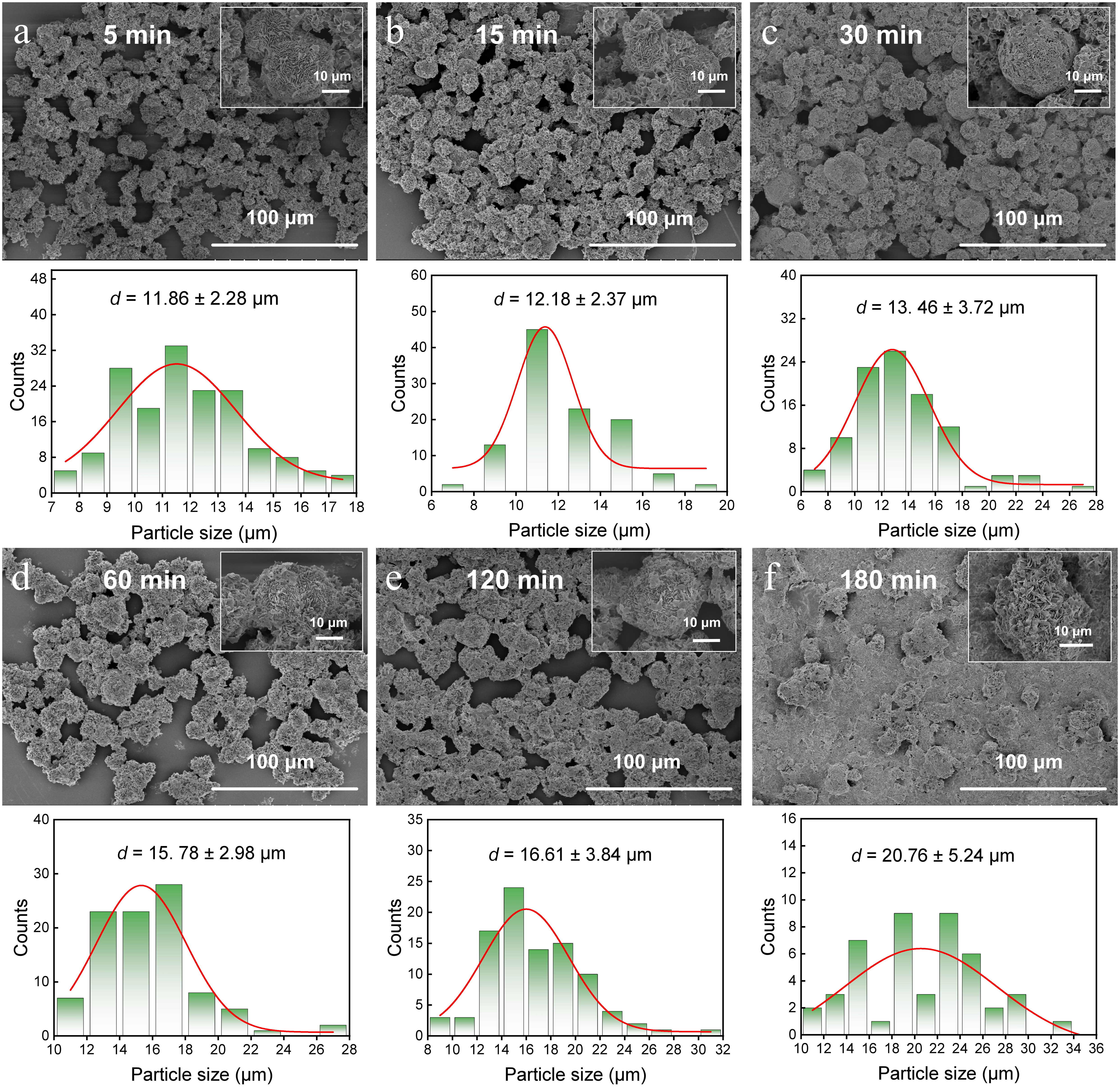
a
5 min
10 μm
100 μm
d = 11.86 ± 2.28 μm
Counts
Particle size (μm)
b
15 min
10 μm
100 μm
d = 12.18 ± 2.37 μm
Counts
Particle size (μm)
c
30 min
10 μm
100 μm
d = 13. 46 ± 3.72 μm
Counts
Particle size (μm)
d
60 min
10 μm
100 μm
d = 15. 78 ± 2.98 μm
Counts
Particle size (μm)
e
120 min
10 μm
100 μm
d = 16.61 ± 3.84 μm
Counts
Particle size (μm)
f
180 min
10 μm
100 μm
d = 20.76 ± 5.24 μm
Counts
Particle size (μm)

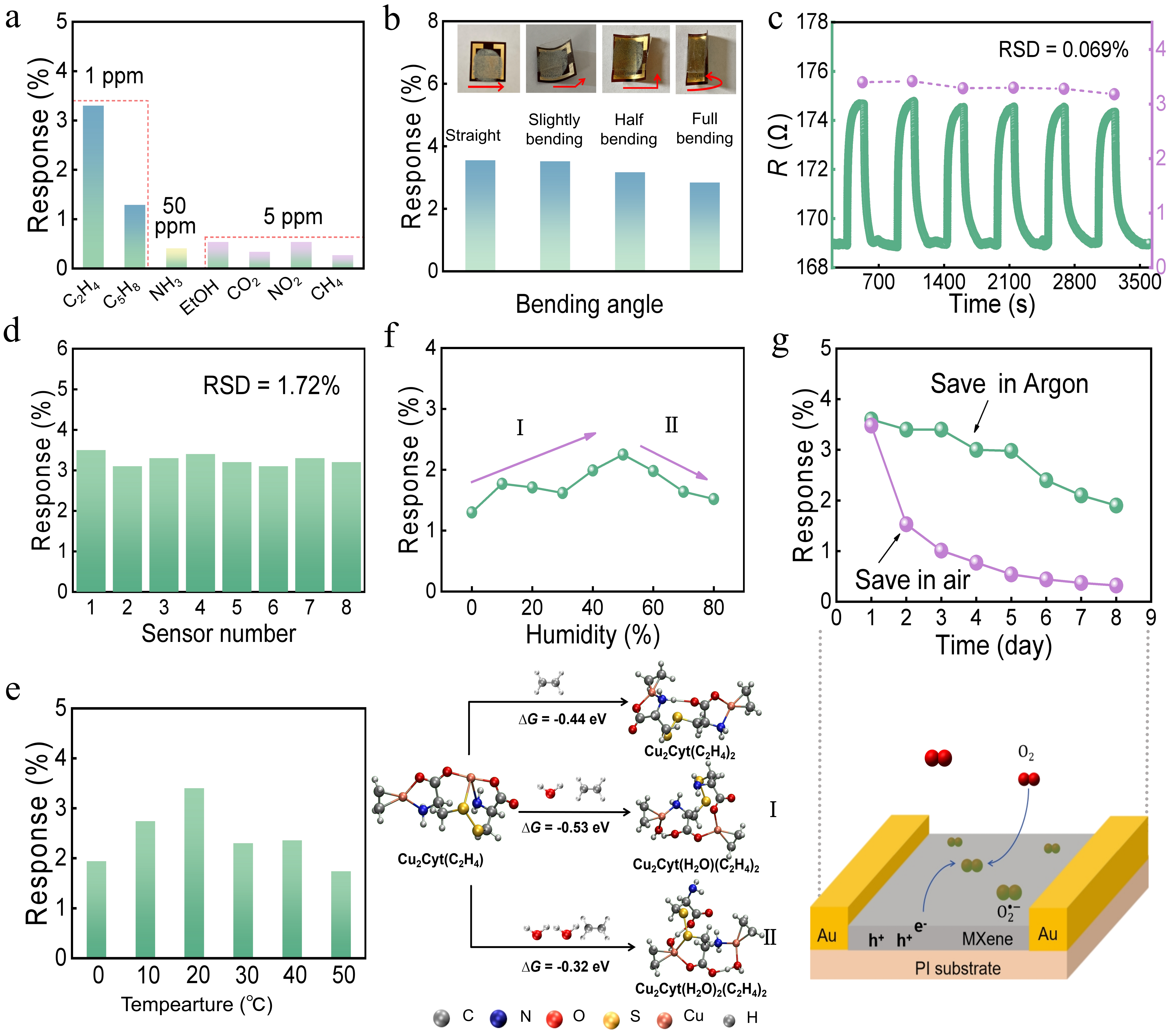
a
Response (%)
1 ppm
50 ppm
5 ppm
C_2H_4
C_5H_8
NH_3
EtOH
CO_2
NO_2
CH_4
b
Response (%)
Straight
Slightly bending
Half bending
Full bending
Bending angle
c
RSD = 0.069%
R (Ω)
Response (%)
Time (s)
700
1400
2100
2800
3500
d
RSD = 1.72%
Response (%)
Sensor number
f
I
II
Response (%)
Humidity (%)
g
Save in Argon
Save in air
Response (%)
Time (day)
e
Response (%)
Tempearture (℃)
ΔG = -0.44 eV
$Cu_2Cyt(C_2H_4)_2$
$Cu_2Cyt(C_2H_4)$
ΔG = -0.53 eV
$Cu_2Cyt(H_2O)(C_2H_4)_2$
I
ΔG = -0.32 eV
$Cu_2Cyt(H_2O)_2(C_2H_4)_2$
II
C
N
O
S
Cu
H
O_2
$O_2^{\bullet-}$
e^-
h^+
h^+
Au
MXene
Au
PI substrate

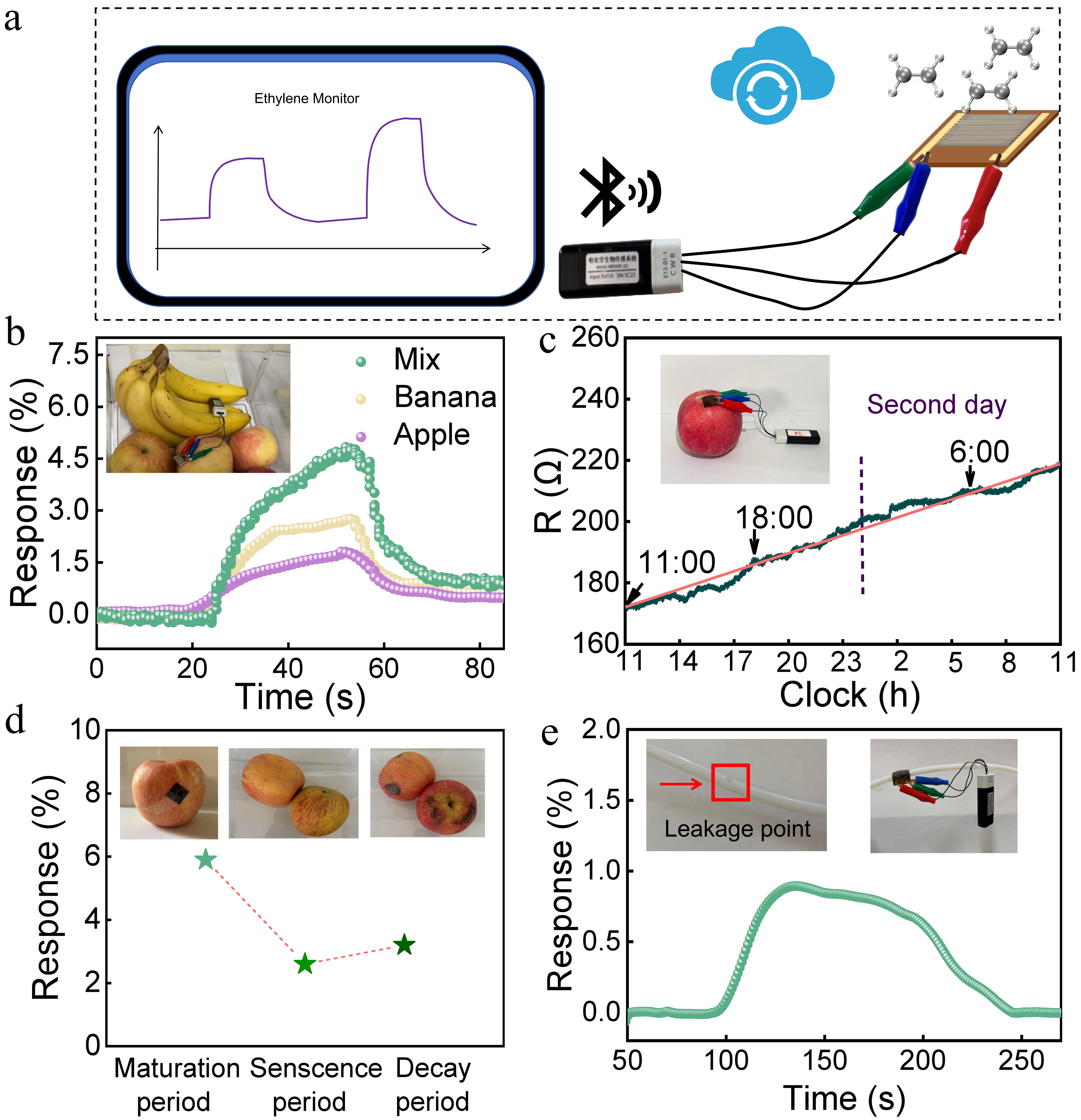
a
Ethylene Monitor
b
Response (%)
7.5
6.0
4.5
3.0
1.5
0.0
Mix
Banana
Apple
0
20
40
60
80
Time (s)
c
260
240
220
200
180
160
R (Ω)
Second day
11:00
18:00
6:00
11
14
17
20
23
2
5
8
11
Clock (h)
d
10
8
6
4
2
0
Response (%)
Maturation period
Senscence period
Decay period
e
2.0
1.5
1.0
0.5
0.0
Response (%)
Leakage point
50
100
150
200
250
Time (s)